

ARTICLE

# Strut-and-tie model for column-to-drilled shaft connections in reinforced concrete bridge columns subjected to lateral loads

Penghui Zhang<sup>1</sup>  | Lianxu Zhou<sup>2</sup> | Junjun Guo<sup>1</sup> | Zhiqiang Wang<sup>1</sup>

<sup>1</sup>Department of Bridge Engineering,  
Tongji University, Shanghai, China

<sup>2</sup>School of Engineering, University of  
British Columbia, Kelowna, British  
Columbia, Canada

## Correspondence

Zhiqiang Wang, Department of Bridge  
Engineering, Tongji University, 1239  
Siping Road, Shanghai 200092, China.  
Email: [wangzhiq@tongji.edu.cn](mailto:wangzhiq@tongji.edu.cn)

## Funding information

National Natural Science Foundation of  
China, Grant/Award Numbers: 51978511,  
51778470, 52308520

## Abstract

Drilled shafts with a larger diameter than columns are frequently adopted as the foundation of highway bridge columns due to their superior economic efficiency and lower impact on existing facilities in the urban built-up area. Different section dimensions lead to a socket connection between the column and the oversized shaft and a noncontact lap splice of their longitudinal bars. The force-transfer mechanism and failure process of column-to-drilled shaft connections were deeply revealed in this study. Detailed FE models were developed at the *Diana* platform and validated against previous experimental results. Subsequently, a parametric study investigated the effect of the shear span-to-depth ratio, diameter ratio of shaft-to-column, column embedment depth, and shaft stirrup ratio. Finally, a modified strut-and-tie model (STM) was proposed to design stirrups of the transition region efficiently considering the experimental failure mechanism. Results indicate that the numerical models built in the *Diana* platform can precisely simulate the mechanical behavior of column-to-drilled shaft connections. The failure mechanism of column-to-drilled shaft connections is shaft stirrups yield at the compressive side induced by extrusion between the embedded column and shaft. The lateral loading capacity of column-to-drilled shaft connections increases with the increase of shear span-to-depth ratio, diameter ratio of shaft-to-column, column embedment depth, and shaft stirrup ratio. The modified STM is able to reveal the variation tendency of shaft transverse reinforcement demand with the various design parameters and give an average stirrup stress ratio of 1.20 and a coefficient of variation of only 8.31%.

## KEYWORDS

column-to-drilled shaft connection, damage mechanism, lateral loading capacity, numerical simulation, socket connection, strut-and-tie model

## 1 | INTRODUCTION

Cast-in-place (CIP) drilled shafts are frequently utilized in highway bridges due to their superior economic

efficiency and lower impact on existing facilities in the urban built-up area.<sup>1,2</sup> For the extended pile shaft supported bridge with consistent diameter and reinforcement between the pile shaft and the column, the

earthquake-induced plastic hinge generally forms on the belowground pile shaft, which is adverse to post-earthquake damage assessment and repair.<sup>3–5</sup> The oversized shaft with a larger diameter than the column is able to shift the plastic hinge to the column while the shaft is undamaged. However, different sectional dimensions lead to a socket connection between the column and the shaft and a noncontact lap splice of their longitudinal bars. A few experimental, numerical, and theoretical studies have been conducted to reveal failure mode and develop design methodology corresponding to various force-transfer mechanisms of column-to-drilled shaft connections.

McLean and Smith<sup>6</sup> developed two- and three-dimensional strut-and-tie models (STMs) for noncontact lap splices. Subsequently, the design equation for shaft stirrups in the transition region (i.e., the connection region of the column and pile shaft) was proposed. A required splice length of  $1.7l_d + s$  was suggested to prevent bond failure of longitudinal column bars, where  $l_d$  denotes the tension development length, and  $s$  denotes the distance between adjacent spliced bars. The design equation was adopted by the AASHTO LRFD specification.<sup>7</sup> Considering the potential effects of strain penetration and split cracks, Caltrans seismic design criteria<sup>8</sup> specifies that the longitudinal bars of a column should be embedded into an oversized shaft with a minimum length of  $D_{\max} + l_d$ , where  $D_{\max}$  denotes the maximum dimension of the column section measured in the longitudinal and transverse directions. The minimum shaft stirrup ratio is also stipulated in Caltrans seismic design criteria. Tran<sup>9</sup> conducted quasi-static tests on three column-to-drilled shaft connection specimens with different shaft stirrup ratios and diameter ratios of shaft-to-columns. The precast column and CIP shaft were integrated through the socket connection. Prying failure was observed in the transition region when shaft stirrups were insufficient. Moreover, the circumferential constraint was provided by concrete in the case of low column drifts. In contrast, the circumferential constraint was mainly provided by the shaft stirrup in the case of high column drifts due to severe concrete cracks in the transition region. The other specimen with a CIP column was consequently tested by Chang,<sup>10</sup> and a similar mechanical behavior as the precast specimen was observed in the transition region. Murcia-Delso et al.<sup>11</sup> reported that the minimum splice length specified in AASHTO and Caltrans specifications was over-conservative based on the result of a series of full-scale experiments and numerical simulations. A splice length of  $l_d + s$  was suggested and validated by experiments. In addition, a steel casing could effectively control tensile splitting cracks in the top of the shaft and improve the anchoring effect of longitudinal bars in the column. Lotfizadeh<sup>12</sup> further investigated the

seismic performance of a specimen with high-strength reinforcement (i.e., Grade 80) on the basis of Murcia-Delso's experiments. Masud<sup>13</sup> investigated the performance of noncontact lap splices in rectangular column-to-drilled shaft connections under the eccentric axial load. It was found that structural stiffness increased with the increase of splice length and decline of splice distance of spliced bars. The noncontact splice distance between spliced bars was recommended to be less than 6 in. (15.24 cm).

Cheng et al.<sup>14</sup> established finite element (FE) models of column-to-drilled shaft connections in the *Abaqus* platform and verified them against Tran's experimental data. Parametric analysis is consequently conducted. And the results indicated that the lateral load strength increased with increasing connection diameter-to-column diameter ratio, column embedment length-to-column diameter ratio, and concrete strength in the transition region. Based on Masud's experiments, Chen et al.<sup>15,16</sup> conducted two-dimensional (2D) and three-dimensional (3D) multiscale analyses of noncontact splices. It was observed that the widest shear crack appears at the end of the overlapped region, almost reaching 45° regardless of splice distance. It is worth noting that the current recognition of the force-transfer mechanism in column-to-drilled shaft connections is insufficient. Analysis models based on the premise significantly underestimated shaft stirrup stress compared to experimental results,<sup>10</sup> which can be attributed to the following drawbacks: (1) the shaft stirrup design generally focuses on the noncontact lap splice requirement of longitudinal bars, which assumes the maximum stirrup stress appears on the tension side of the shaft section. However, the shaft stirrup first yields at the compressive side induced by extrusion between the embedded column and shaft, as described in Section 3.4; (2) the nonuniform stress distribution along the stirrup circumference has not been considered; (3) the inclination of diagonal struts between spliced bars is significantly overestimated in existing models. Experimental investigations and multiscale numerical analyses have shown that it is actually approximately 45°.

To address the limitations of existing analysis models and provide a more comprehensive understanding of the force-transfer mechanism and failure process of column-to-drilled shaft connections, this study employs a multi-faceted approach. Firstly, detailed FE models were developed using the *Diana* platform and validated against previous experimental results, offering a robust numerical tool for investigating the connection behavior. Secondly, a comprehensive parametric study was conducted to systematically evaluate the effects of key design parameters, including the shear span-to-depth ratio, diameter ratio of shaft-to-column, column embedment depth, and shaft stirrup ratio. This extensive investigation provides

valuable insights into the influence of these parameters on the connection performance, which has not been thoroughly explored in previous research. Finally, based on the experimental observations and numerical findings, a modified STM is proposed for the efficient design of shaft stirrups in the transition region. The novelty of the proposed STM lies in its incorporation of the realistic failure mechanism and its ability to provide a more accurate representation of the force-transfer mechanism compared to existing models. The outcomes of this study are expected to advance the current understanding of column-to-drilled shaft connections and provide practical guidance for their design, ultimately contributing to the development of safer and more resilient bridge structures.

## 2 | EXISTING ANALYSIS MODELS FOR COLUMN-TO-SHAFT CONNECTION

To form a stable plastic hinge at the column base without inducing damage in the transition region, two conditions must be fulfilled: (1) the splice length of longitudinal bars, as shown in Figure 1, should be sufficient to prevent bond failure of themselves; (2) adequate stirrups are required in the transition region to avoid prying failure. McLean and Smith<sup>6</sup> proposed a 2D-STM based on the experimental data of flat panel specimens under pure tensile load, as shown in Figure 1a. In this model, the tensile stress of longitudinal bars was considered to transfer through the concrete diagonal struts with an inclination  $\theta$  of  $45^\circ$ . The required spacing of stirrups for the flat panel was determined by Equation (1), ignoring the tensile strength of the concrete.

$$s_{tr} = \frac{A_{tr} f_{ytr} l_s}{A_l f_{ul}}, \quad (1)$$

where  $A_{tr}$  and  $f_{ytr}$  are the area and yield strength of transverse reinforcements, respectively;  $A_l$  and  $f_{ul}$  are the area and ultimate strength of longitudinal bars, respectively;  $l_s$  represents the required splice length of longitudinal bars. Furthermore, they developed a 3D-STM to predict the stirrup requirement of the column-to-drilled shaft connection under pure tensile load, as illustrated in Figure 1b. The maximum spacing of the stirrup was given as:

$$s_{tr} = \frac{2\pi A_{tr} f_{ytr} l_s}{A_l f_{ul}}, \quad (2)$$

It is worth noting that Equation (2) could only be valid when the specimen is subjected to pure tension load. In this load condition, all spliced bars are in a tension state. However, bridge columns usually suffer both axial and lateral loads during earthquakes, which means that the longitudinal bars experience compression and tension depending on the location of the bars. In this regard, AASHTO LRFD specification<sup>7</sup> modified Equation (2) as:

$$s_{tr} = \frac{2\pi A_{tr} f_{ytr} l_s}{k A_l f_{ul}}, \quad (3)$$

where  $k$  is the factor representing the ratio of the column's tensile reinforcements to total column reinforcements at the nominal resistance. For simplification,  $k$  can be conservatively taken a default value of 0.5.

Murcia-Delso et al.<sup>11</sup> noticed that Equation (1) and Equation (2) were developed based on the assumption that the bond stress was distributed uniformly along the effective lap length. This assumption may be reasonable for reinforcing bars with a short embedment length of three to five times the reinforcement diameter. However, the bond stress distribution is highly nonuniform for longitudinal column bars with a longer embedment length.<sup>17</sup> Based on experimental results, Mains<sup>18</sup> pointed out that

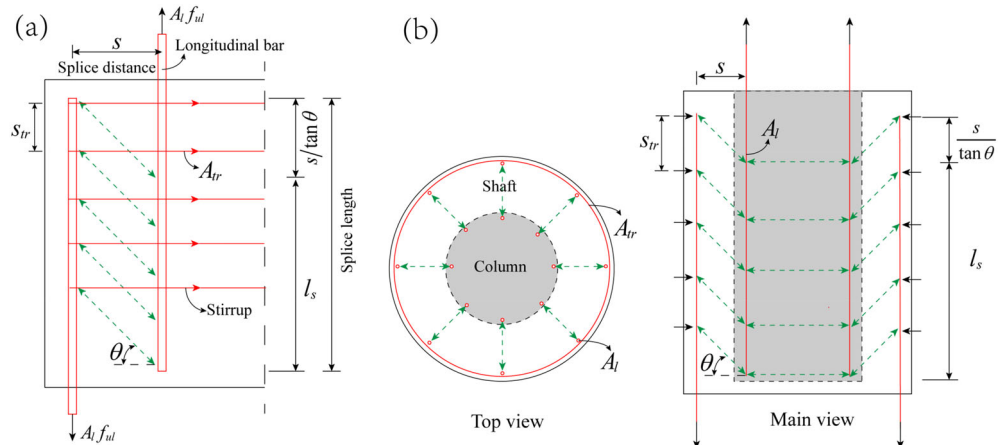


**FIGURE 1** Strut-and-tie models proposed by McLean and Smith<sup>6</sup> for pure tension load: (a) 2D-STM for flat panel specimen; (b) 3D-STM for column-to-drilled shaft connection. STM, strut-and-tie model.

the maximum local bond stress could be larger than twice its average value. Therefore, Murcia-Delso et al. determined the minimum shaft stirrup requirement based on the local bond stress of column bars. The analysis model is shown in Figure 2. Taking the equilibrium of free bodies ABEF and BCDE, as indicated in the right part of Figure 2, the maximum stirrup spacing to avoid bond failure can be determined as Equation (4) in a condition that the bond stress is conservatively considered as the maximum bond strength  $\tau_{\max}$ .

$$s_{\text{tr}} = \frac{2\pi A_{\text{tr}} f_{\text{ytr}}}{N_{\text{col}} \tau_{\max} d_{\text{col}}}, \quad (4)$$

where  $N_{\text{col}}$  is the total number of longitudinal column bars.

Similar to McLean and Smith's model, Murcia-Delso's model is over-conservative for column-to-drilled shaft connections under lateral load since the maximum bond stress of longitudinal column bars will not appear at the same depth. Tran<sup>9</sup> developed a STM for the transition region under axial and lateral loads, as illustrated in Figure 3. The compression concrete struts and tension ties are denoted by dashed green lines and solid red lines, respectively. In this model, the resultant tensile forces of column and shaft are denoted as  $T_c$  and  $T_s$ , respectively, and the resultant compressive forces of column and shaft are denoted as  $C_c$  and  $C_s$ , respectively. The boundary forces and their locations are determined by sectional moment-curvature analysis.  $V$  is the shear force;  $L$  represents the length of the transition region. Based on experimental results, the strain of shaft stirrups is distributed parabolically in the vertical direction. The centroid of the stirrup force is located 1/4 down the transition length from the top of the transition region. The resultant force of shaft stirrups can be written as:

$$F_{\text{tr}} = F_{\text{BC}} = \frac{T_s}{\tan \theta}. \quad (5)$$

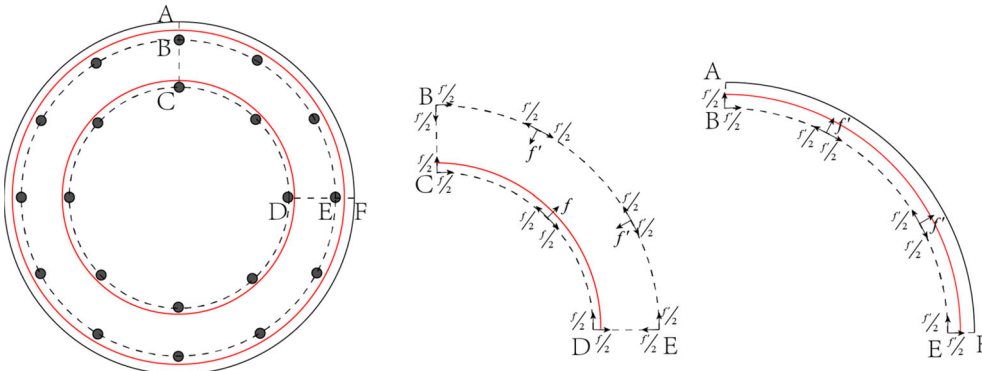


FIGURE 2 Mechanical model proposed by Murcia-Delso et al.<sup>11</sup>

Equation (5) indicates that the resultant stirrup force  $F_{\text{tr}}$  totally depends on the inclination of the strut AB, which emphasizes the importance of accurate prediction of the point A position. Tran<sup>9</sup> thought point A should locate a distance of  $l_d + s + c - l_{d,\text{eff}}/2$  below the top of the transition region, where  $l_{d,\text{eff}}$  is the effective anchorage length of the column bars.

Chang<sup>10</sup> modified Tran's model, as shown in Figure 4, so as to simulate the force-transfer mechanism of the transition region more accurately. Comparing the magnitude of the horizontal component of the strut CD to the shear force  $V$ , the STM can be separated into shear-dominant mode and moment-dominant mode. The transition depth  $L$  is revised to the development length of longitudinal column bars:

$$L = \min \{ l_d + \sqrt{3} e_{\text{ef}} + c, l_e \}, \quad (6)$$

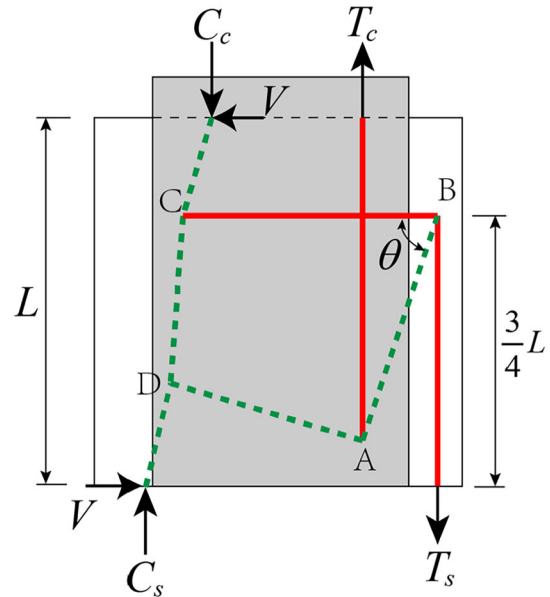
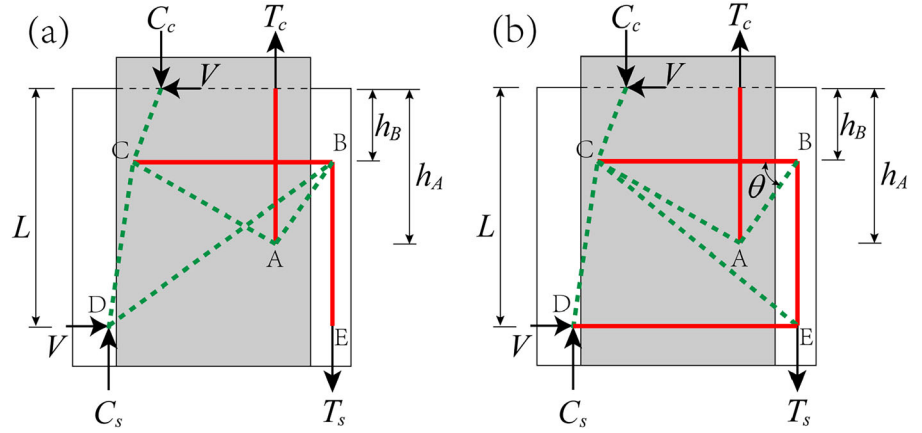


FIGURE 3 Strut-and-tie model proposed by Tran.<sup>9</sup>

**FIGURE 4** Strut-and-tie model proposed by Chang<sup>10</sup>: (a) shear-dominant mode; (b) moment-dominant mode.



where  $e_{ef}$  is the horizontal distance between  $T_c$  and  $T_s$ ;  $l_e$  is the embedment depth of the column. In Equation (6), the inclination of concrete diagonal struts between spliced bars is set to  $60^\circ$  at the end of spliced bars. The position of point A is set as the center of development length of column bars while uniform bond stress distribution is assumed:

$$h_A = \begin{cases} l_d/2 + \sqrt{3}e_{ef} + c, & l_e > l_d + \sqrt{3}e_{ef} + c \\ (l_e - \sqrt{3}e_{ef} - c)/2, & l_e \leq l_d + \sqrt{3}e_{ef} + c \end{cases} \quad (7)$$

Point B is located at the centroid of the stirrup force or half the development length of the longitudinal shaft bars. It was thought that the tie force  $F_{BC}$  represents all transverse ties acting radially in the tensile side of the section. The resultant force of shaft stirrups is determined by Equation (8).

$$F_{tr} = V + \frac{2}{\pi}(F_{BC} - V). \quad (8)$$

Tran's model and Chang's model determined the inclination of strut AB by the locations of points A and B, leading to a  $\theta$  usually greater than  $60^\circ$ . However, the inclination of diagonal struts between spliced bars is approximately  $45^\circ$ , following the experimental investigation and multiscale numerical analysis.<sup>16,19</sup>

### 3 | NUMERICAL SIMULATION AND VALIDATION

#### 3.1 | Description of selected experiments

In order to deeply reveal the force-transfer mechanism and failure process of the transition region, numerical

simulation is conducted for specimens DS2 and DS4 tested at the University of Washington, which are the only two specimens exhibited prying failure in the transition region instead of column flexural failure among existing experimental studies.<sup>9-13,20</sup> The pseudo-static tests of these two specimens are accomplished by Tran<sup>9</sup> and Chang,<sup>10</sup> respectively.

As shown in Figure 5, these two 1/3.6 scaled specimens had identical configurations, which consisted of the column, shaft, and footing. The column has a diameter of 508 mm. The loading point is located at 1524 mm above the shaft top, resulting in a shear span-to-depth ratio of 3.0. The column embedment length is 711 mm, which equals 1.4 times the column diameter. The shaft diameter is 762 mm, and the diameter ratio of shaft-to-column is 1.5. The shaft height is set as the length from the inflection point of the pile shaft to the pile top, which is approximately 1.5 times the column diameter. The column longitudinal reinforcement ratios of specimens DS2 and DS4 are 0.99% and 1.58%, respectively. The ends of longitudinal column bars in specimen DS2 are terminated with mechanical anchor heads. But the bar strain is about zero near the anchors in accordance with experiment results, which indicates the anchor heads are not necessary. Therefore, anchors are eliminated in specimen DS4. The shaft longitudinal reinforcement ratios of specimens DS2 and DS4 are 0.93% and 2.04%, respectively. The splice length of the longitudinal bars between the column and shaft is 660 mm, which equals 42 times the bar diameter and meets the requirement of AASHTO LRFD specification.<sup>7</sup> The 9-gauge wire stirrup spacing is 76 mm and 19 mm in the shafts of specimens DS2 and DS4, corresponding to a volumetric stirrup ratio of 0.09% and 0.35%, respectively. Moreover, the shaft spirals are densified with three and six turns at the shaft top of specimens DS2 and DS4.

The material properties of steel bars and concrete are listed in Table 1 and Table 2, respectively. In Table 1,  $f_y$



and  $f_u$  represent the yield strength and ultimate strength of steel bars. The yield strength of the wire is not given in material tests; the nominal yield strength (482.7 MPa) is adopted in the numerical analysis.<sup>21</sup>

### 3.2 | Description of numerical model

The 3D numerical models of the selected specimens described previously were generated in the *Diana* platform, as illustrated in Figure 6. The concrete was

modeled with linear hexahedron elements, and the reinforcement was simulated using truss elements. A multi-directional rotating smeared crack model was adopted to simulate concrete behavior incorporating compression, tension, and cracking. The compressive constitution of concrete is determined based on the Maekawa model.<sup>22</sup> The triaxial stress-strain relationship is modified on the uniaxial one by the method proposed by Selby and Vecchio.<sup>23</sup> The tension softening process is simulated with the nonlinear softening curve, according to Hordijk.<sup>24</sup> The elastic modulus  $E_c$ , tensile strength  $f_t$ , and fracture energy  $G_f$  can be determined by the mean value of cylinder compressive strength  $f_c$  following the specification in fib Model code<sup>25</sup>:

$$E_c = 21.5 \times (f_c/10)^{1/3}, \quad (9)$$

$$f_t = 0.21 \times (f_c - 8)^{2/3}, \quad (10)$$

$$G_f = 0.073 \times f_c^{0.18}. \quad (11)$$

Steel reinforcements were modeled with the constitutive model proposed by Dodd and Restrepo-Posada<sup>26</sup> to consider yield platform and parabolic strengthening. The local bond-slip relationship between concrete and reinforcing bars was simulated according to the constitution specified in fib Model code.<sup>25</sup> The bond stress can be attributed to friction and mechanical interlocking between ribs and surrounding concrete with respect to deformed hot-rolled ribbed steel bars. For smooth bars, bond stress is provided only by the friction mechanism.

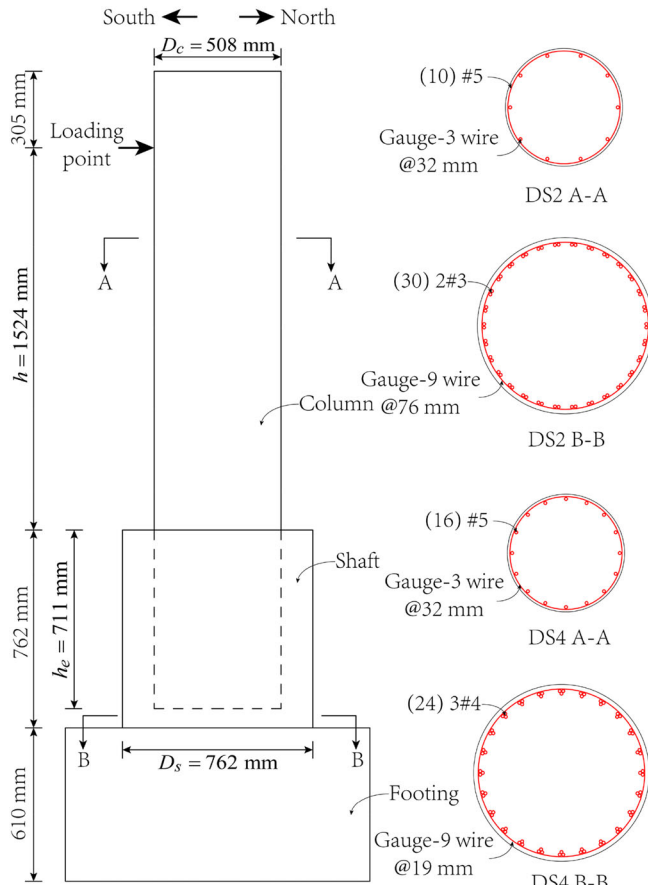


FIGURE 5 Details of specimens.

TABLE 2 Measured concrete cylinder compressive strength for specimens.

	Column (MPa)	Shaft and footing (MPa)
DS2	49.4	44.5
DS4	48.9	46.2

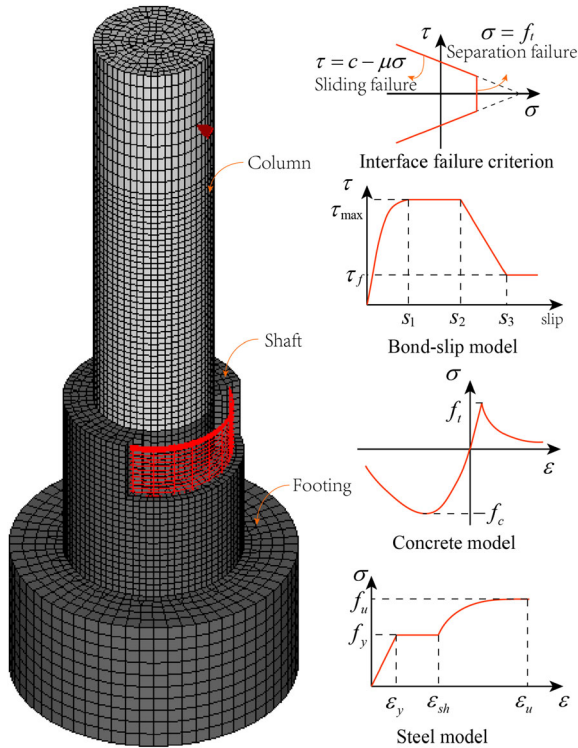
	Longitudinal column bars	Column stirrups	Longitudinal shaft bars	Shaft stirrups
DS2				
$f_y$ (MPa)	463.3	482.7 <sup>a</sup>	454.4	482.7 <sup>a</sup>
$f_u$ (MPa)	735.7	655.3	702.6	757.5
DS4				
$f_y$ (MPa)	448.2	482.7 <sup>a</sup>	475.8	482.7 <sup>a</sup>
$f_u$ (MPa)	661.9	717.1	675.7	675.7

TABLE 1 Measured reinforcement strength for specimens.

<sup>a</sup>The nominal yield strength specified in the American Society for Testing and Materials Standard A82.

Parameters for defining the bond stress–slip relationship of deformed bars are listed in Table 3. For specimen DS2 with a precast column, the effect of the interface between the precast column and the shaft is considered by introducing a Coulomb friction interface in the model to simulate potential sliding. The modified Coulomb failure criterion with a coefficient of friction  $\mu$  of 0.6 and a

cohesion  $c$  of  $0.28f_c$  is adopted for interface elements.<sup>27</sup> Considering that the footing and column body around the loading point remained elastic during the test, the mesh size was only densified in plastic zones due to computational efficiency. The bottom surface of the footing was fixed. A vertical load of 707 kN was applied to the top of the column, corresponding to  $0.1f_cA_g$ , where  $A_g$  is the gross section area of columns. Subsequently, a lateral displacement-controlled monotonic load was applied to the loading point with a loading step of 1.5 mm. The regular Newton–Raphson method was employed in nonlinear structural analysis considering geometric nonlinearity with convergence criteria based on displacement and internal energy.



**FIGURE 6** Configuration and mesh density of the numerical models.

### 3.3 | Numerical model validation

The FE model was validated against experimental results. Considering that the present study mainly focuses on the mechanical behavior of the transition region, the verification was conducted by comparing the experimental and numerical response with the column drift ratio less than 3.0%, which was consistent with the proceeding of Cheng et al.<sup>14</sup> On the one hand, the rotating crack approach is unsuitable for concrete simulation with severe crack width. On the other hand, ductility design criteria require the transition region to remain elastic when a plastic hinge forms in the column. The loads applied to the transition region were no longer significantly changed after the column drift ratio reached 3.0% due to the plastic hinge mechanism. Thus, the selected range of column drift ratio is sufficient to reveal the seismic performance

**TABLE 3** Parameters for bond stress–slip curves.

	Longitudinal column bars	Longitudinal shaft bars	Column stirrups	Shaft stirrups
DS2				
$\tau_{\max}$ (MPa)	16.08	7.55	0.32	0.30
$\tau_f$ (MPa)	6.43	3.02	0.32	0.30
$s_1$ (mm)	1	1.8	0.01	0.01
$s_2$ (mm)	2	3.6	0.01	0.01
$s_3$ (mm)	10.6	6.2	0.01	0.01
DS4				
$\tau_{\max}$ (MPa)	15.99	7.73	0.32	0.31
$\tau_f$ (MPa)	6.39	3.09	0.32	0.31
$s_1$ (mm)	1	1.8	0.01	0.01
$s_2$ (mm)	2	3.6	0.01	0.01
$s_3$ (mm)	10.6	8.3	0.01	0.01

of column-to-drilled shaft connections, such as strength and stiffness.

The experimentally-measured and numerically-simulated backbone curves are compared in Figure 7. It is observed that the numerical backbone curves match well with the experimental ones. It is worth noting that the numerically-simulated force of specimen DS2 near the drift ratio of 1.0% was slightly dropped, which could be attributed to the modulus of reinforcing bars being less than the softening modulus of concrete, leading to a negative overall sectional stiffness. In addition, a mesh sensitivity analysis was conducted to study the influence of mesh sizes on numerical results. The numerical results corresponding to element sizes of 20 mm and 30 mm agree well with each other, indicating the negligible effect of mesh sensitivity. To balance computational efficiency and accuracy, a 60 mm mesh size was used for 304.8 mm (12 in.) above and below the loading points and for the foundation. The column's plastic region was simulated with a mesh size equal to 30 mm, while the mesh size of shafts was set as  $\min\{30, (D_s - D_c)/8\}$ , where  $D_s$  and  $D_c$  denote the diameters of the shaft and column, respectively.

The simulation result indicates that specimens DS2 and DS4 exhibit identical damage development processes, as illustrated in Figure 8. Horizontal flexural cracks appeared at the column bottom and transition region

first. With the increase of lateral load, radial splitting cracks appeared on the tensile side of the shaft due to the increasing bond stress of longitudinal column bars, and vertical cracks appeared on the compressive side owing to the horizontal shear force. Cracks developed, widened, and connected, followed by the yielding of longitudinal column bars and shaft stirrups. The experimental and numerical drift ratios of DS2 (DS4) corresponding to the yielding of longitudinal column bars are 0.7% and 0.58% (0.8% and 0.7%), respectively. In comparison, the ones corresponding to the yielding of shaft stirrups are 1.5% and 1.92% (2.0% and 2.6%). Figure 9 shows the numerical crack distribution corresponding to a drift ratio of 3.0%, which agrees well with the crack distribution recorded in the experiment. Moreover, the comparison of numerical and experimental reinforcement strain at different drift levels is illustrated in Figure 10. The reference depth of 0.0 m is set at the interface between the column and shaft. The difference between numerical and experimental results could mainly be attributed to the ignorance of bond strength reduction because of reinforcement yielding and concrete cracking. As a result, the difference is more remarkable for longitudinal bars since the ribbed longitudinal bars suffered a more significant influence of bond-slip effects than smooth stirrups. This omission was adopted to balance computational efficiency and model versatility. While these local effects may influence

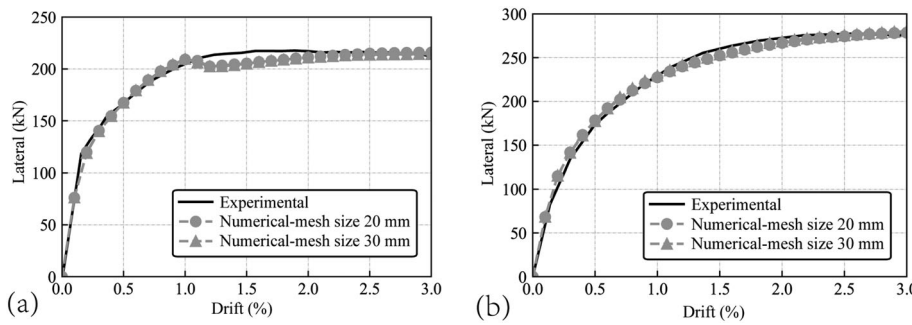


FIGURE 7 Comparison of backbone curves: (a) DS2; (b) DS4.

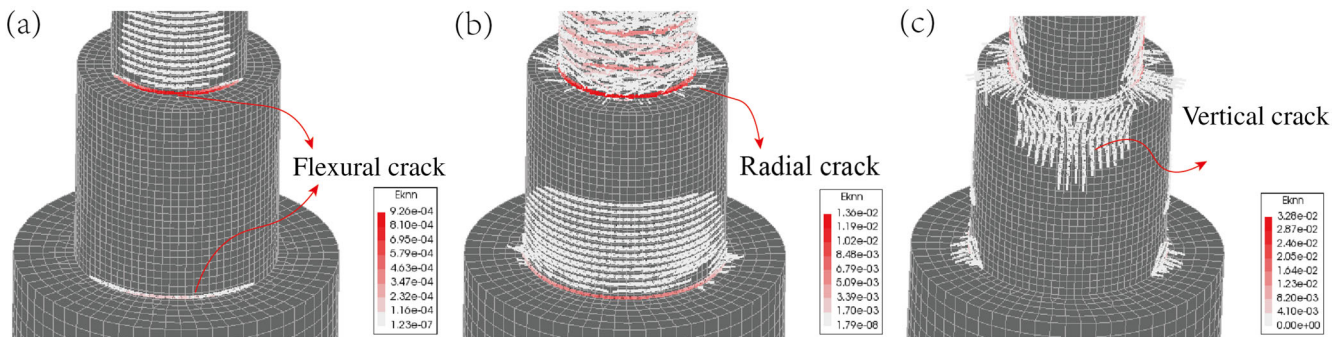


FIGURE 8 Damage progression: (a) flexural cracks at the column bottom and transition region; (b) radial splitting cracks on the tensile side of the shaft; (c) vertical cracks on the compressive side of the shaft.



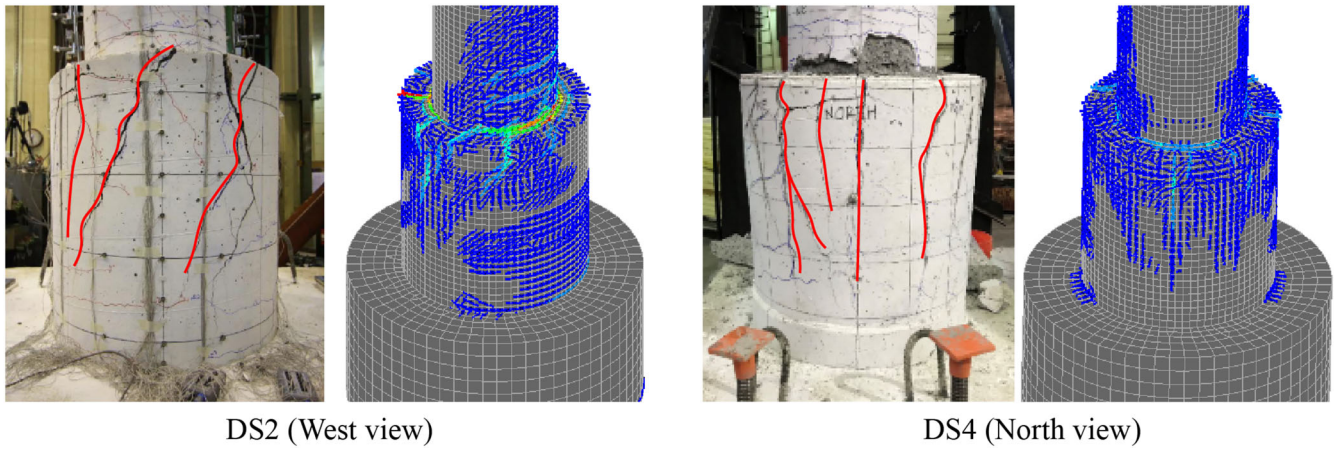


FIGURE 9 Comparison of crack distribution under north-south loading direction.

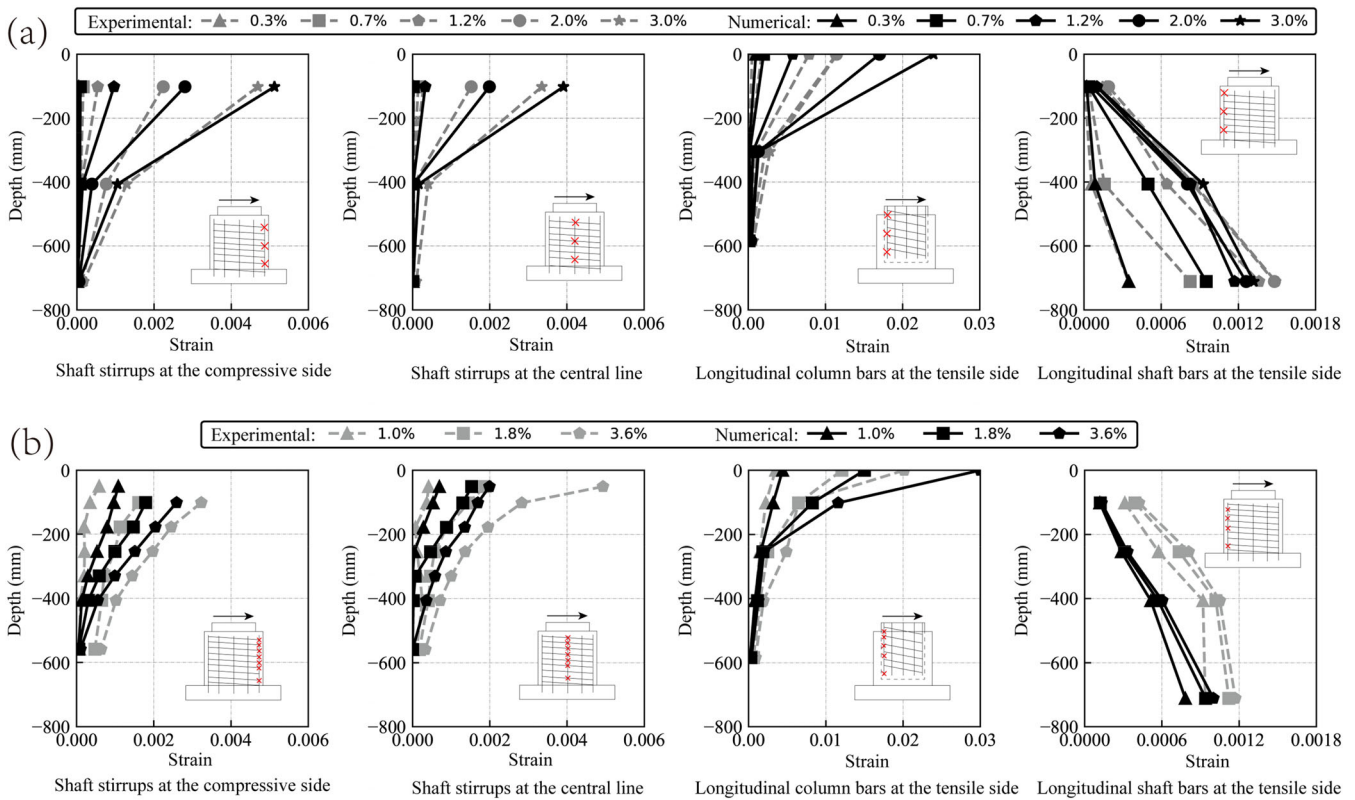


FIGURE 10 Comparison of numerical and experimental bar strain with various drifts: (a) DS2; (b) DS4.

bond strength, this study focuses primarily on the structure's global behavior. As shown in Figure 7, the comparison of backbone curves between numerical and experimental results demonstrates that despite this omission, the finite element model still captures the overall structural behavior reasonably well. It is worth noting the significant difference between measured and simulated shaft stirrup strain corresponding to a drift ratio of 3.6% in Figure 10b, which could be attributed to the severe concrete cracking in the transition region. Due to

the strain concentration of shaft stirrups near concrete cracks, the measured stirrups strain is obviously greater than the computed one.

### 3.4 | Damage mechanism of column-to-drilled shaft connections

As described in Section 2, existing analysis models attributed the failure of the transition region to shaft stirrup

yielding at the tensile side induced by noncontact lap splice of longitudinal bars. In these existing models, the failure mode of the transition region subjected to seismic loads was considered consistent with that under the pure tensile load. The stirrup stress distribution at the top of the shaft of specimen DS4 is exhibited in Figure 11. When longitudinal column bars first yield at a drift ratio of 0.9%, the hoop constraint for the embedded column at the tensile side is provided by the uncracked shaft concrete. As a result, the tensile stress of the shaft stirrup is very small on the tensile side. On the compressive side, stirrup stress reaches the peak value in the front of the loading direction due to horizontal extrusion between the embedded column and shaft. When shaft stirrups first yield at a drift ratio of 1.7%, the hoop constraint is mainly provided by shaft stirrups since concrete cracks are fully developed. And the peak value of stirrup stress still appears in the front of the loading direction at the compressive side. The test result reported by Tran<sup>9</sup> and Chang<sup>10</sup> also indicates that the stirrup strain at the compressive side is larger than the one at the tensile side, as illustrated in Figure 12. The FE analysis results show that the failure mode of the transition region assumed by existing analysis models is discrepant with the experimental situation. The experimental failure mechanism is shaft

stirrups yield at the compressive side induced by extrusion between the embedded column and shaft.

Another consequence of attributing transition failure to the longitudinal bar splicing is that the flexural capacity of the column-to-drilled shaft connection is independent of the shear span-to-depth ratio of the column. FE models with various shear span-to-depth ratios (i.e., 3, 6, 9) were established to study the effects of shear span-to-depth ratio, denoted as models S1, S2, and S3. These three models have a shaft diameter of  $1.3D_c$ , and the other design parameters are the same as specimen DS4. The moment–drift responses for three considered cases are illustrated in Figure 13. Considering the  $P$ – $\Delta$  effect, the moment at the bottom of the column is given by:

$$M = Fh + P\Delta \frac{H}{h}, \quad (12)$$

where  $M$  is the moment at the column base;  $H$  denotes the height of the column;  $h$  represents the distances from the column base to the loading point;  $P$  and  $F$  are vertical and lateral loads, respectively.

If the first yielding of shaft stirrups triggers the ultimate limit state, Figure 13 implies that the flexural capacity of the column-to-drilled shaft connection increases with the increase of the shear span-to-depth ratio. The

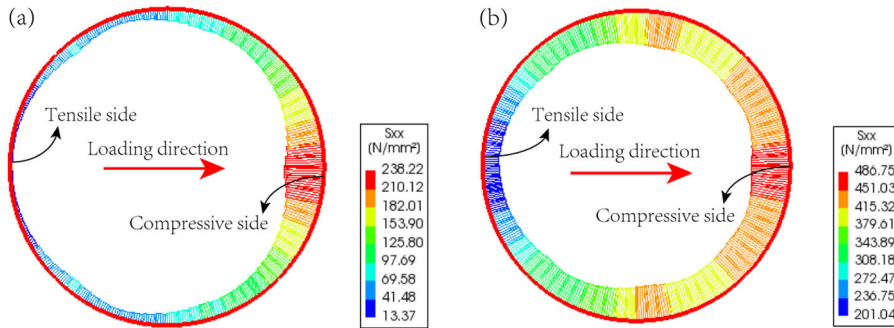


FIGURE 11 Stress distribution of the stirrup at the top of shaft: (a) first yielding of longitudinal column bars; (b) first yielding of shaft stirrups.

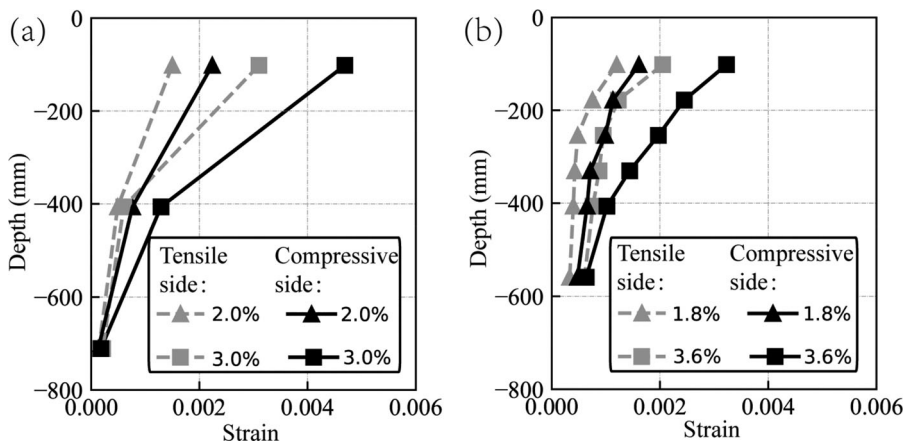


FIGURE 12 Comparison of shaft stirrup strain in tension side and compressive side: (a) DS2; (b) DS4.

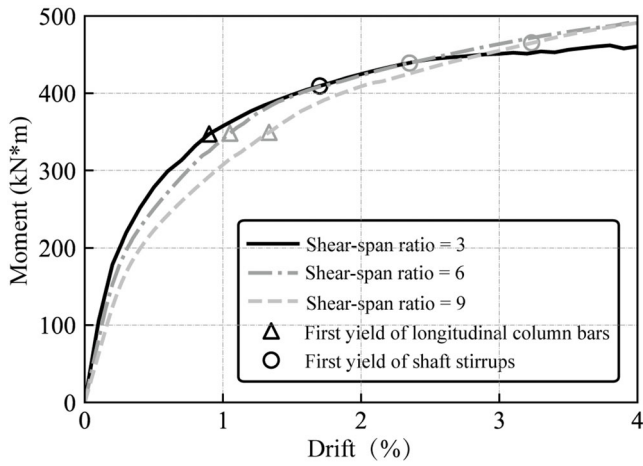


FIGURE 13 Comparison of column moment-drift responses for the models with various shear span-to-depth ratios.

flexural capacity corresponding to models with shear span-to-depth ratios of 6 and 9 is 7.3% and 13.7% higher than the model with a shear span-to-depth ratio of 3, respectively. The ultimate drift ratios of models with shear span-to-depth ratios of 3, 6, and 9 are 1.70%, 2.35%, and 3.23%, respectively.

#### 4 | PARAMETRIC ANALYSIS

Based on the validated FE models, an in-depth parametric analysis was subsequently carried out to investigate the effects of the following parameters on the mechanical behavior of column-to-drilled shaft connections, including: (1) the diameter ratio of shaft-to-column  $D_s/D_c$ ; (2) the column embedment depth  $h_e$ , as indicated in Figure 5; (3) the shaft stirrup ratio among the transition region  $\rho_{tr}$ . Twelve studied scenarios were generated based on specimen DS4 which is regarded as the benchmark scenario, as listed in Table 4. Nonlinear statistic analysis was conducted for each selected scenario. The effective stiffness  $K_{eff}$  and the lateral loading capacity  $F_{max}$  of each selected scenario were calculated and listed in Table 4. The  $K_{eff}$  and  $F_{max}$  corresponds to the first yielding of longitudinal column bars and the first yielding of shaft stirrups, respectively.

##### 4.1 | Diameter ratio of shaft-to-column

Four FE models (i.e., denoted as A1, A2, A3, and A4) were generated in the *Diana* platform, which corresponds to diameter ratios of shaft-to-column equal to 1.2, 1.4, 1.6, and 1.8, respectively, as listed in Table 4. Among these four cases, the A1 to A3 presents the prying failure

TABLE 4 Details of considered cases.

Case	$D_s/D_c$	$h_e$	$\rho_{tr}$ (%)	$K_{eff}$ (kN/mm)	$F_{max}$ (kN)
A1	1.2	$1.4D_c$	0.35	14.59	255.14
A2	1.4	$1.4D_c$	0.35	16.82	266.90
A3	1.6	$1.4D_c$	0.35	20.30	275.10
A4	1.8	$1.4D_c$	0.35	22.92	284.84*
B1	1.3	$0.5D_c$	0.35	\	189.89
B2	1.3	$0.8D_c$	0.35	14.62	234.50
B3	1.3	$1.1D_c$	0.35	14.88	252.20
B4	1.3	$1.4D_c$	0.35	16.19	254.20
C1	1.3	$1.4D_c$	0.28	16.15	249.43
C2	1.3	$1.4D_c$	0.40	16.26	263.59
C3	1.3	$1.4D_c$	0.53	16.37	272.88
C4	1.3	$1.4D_c$	0.81	16.52	285.80*

Note: The value of  $F_{max}$  marked with “\*” represents that the column behaves flexural failure instead of prying failure.

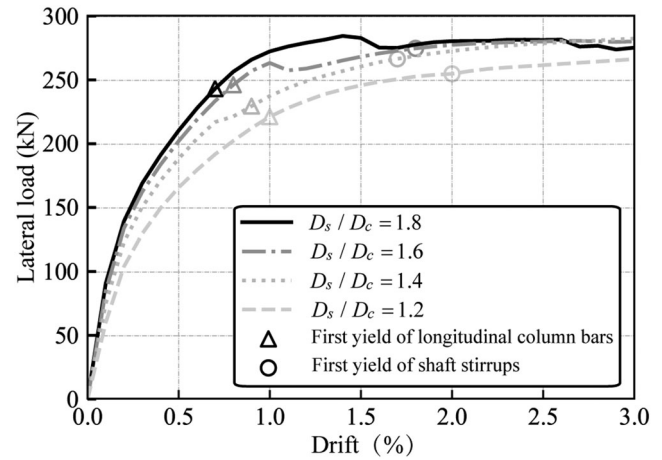


FIGURE 14 Comparison of backbone curves with various diameter ratios of shaft-to-column.

in the transition region, while the remaining A4 presents the flexure failure of the column, and the plastic hinge forms at the bottom of the column. The corresponding backbone curves are shown in Figure 14. It is worth noting that A4 reaches the maximum lateral loading capacity at a drift ratio of 1.5%; however, the maximum stress of the shaft stirrup equal to 404.55 MPa appears at a drift ratio of 2.7%. This phenomenon indicates that the stirrup stress of the shaft is affected by the sectional stress redistribution of the column base. The ductility design of column-to-drilled shaft connection requires that the column ductility is fully utilized and the transition region remains elastic. In this regard, shaft stirrups should not yield until the longitudinal column reinforcements

fracture or core column concrete crushing. Therefore, it is necessary to consider the limit state of maximum displacement ductile<sup>28</sup> during the ductility design of column-to-drilled shaft connection. The effective stiffness rises by 15.3% and 39.1% when the diameter ratio of shaft-to-column increases from 1.2 to 1.4 and 1.6. Once the value of  $D_s/D_c$  is greater than 1.6, the effect of the diameter ratio of shaft-to-column on the effective stiffness is insignificant since the column dominates structure stiffness. In addition, Figure 15 shows the shaft stirrup stress distribution in the front of the loading direction at the time of the first yielding of shaft stirrups. The reference depth of 0.0 m is set at the interface between the column and shaft. The stirrup stress distributes parabolically at diameter ratios of shaft-to-column equal to 1.2 and 1.4, while a linear distribution is observed for a diameter ratio of 1.6.

#### 4.2 | Column embedment depth

Figure 16 compares the backbone curves of the cases with different embedment depths. To suffice the minimum anchorage length requirement of AASHTO LRFD specification, 90-degree hocks are set at the ends of longitudinal column bars of cases B1, B2, and B3. Yielding of longitudinal column reinforcements is not observed in case B1 with an embedment depth of  $0.5D_c$ , and its lateral loading capacity is 25.3% lower than that of case B4 with a depth of  $1.4D_c$ . When the embedment depth is beyond  $1.1D_c$ , the effect of the embedment depth on the lateral loading capacity is insignificant. Moreover, shaft stirrup stress distribution is illustrated in Figure 17. The stirrup stress distributes parabolically among the

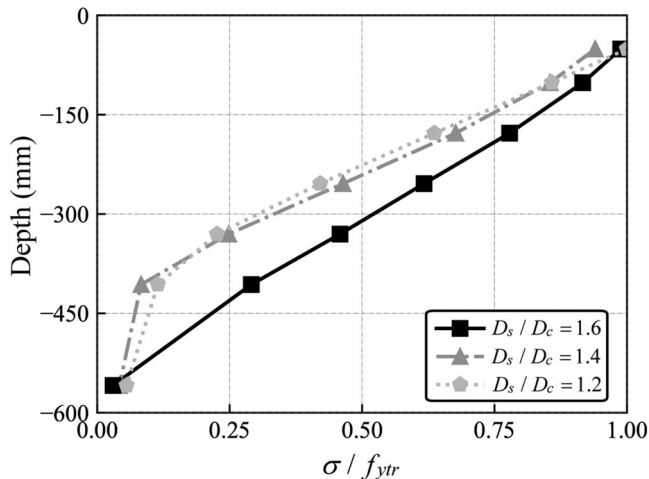


FIGURE 15 Comparison of stress distribution of shaft stirrups with various diameter ratios of shaft-to-column.

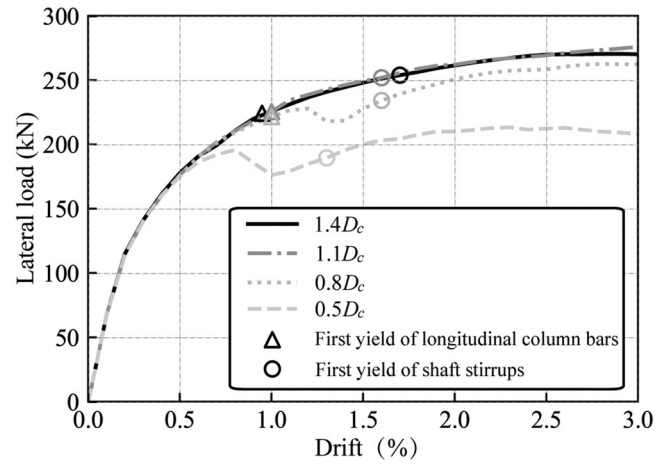


FIGURE 16 Comparison of backbone curves with various embedment depths.

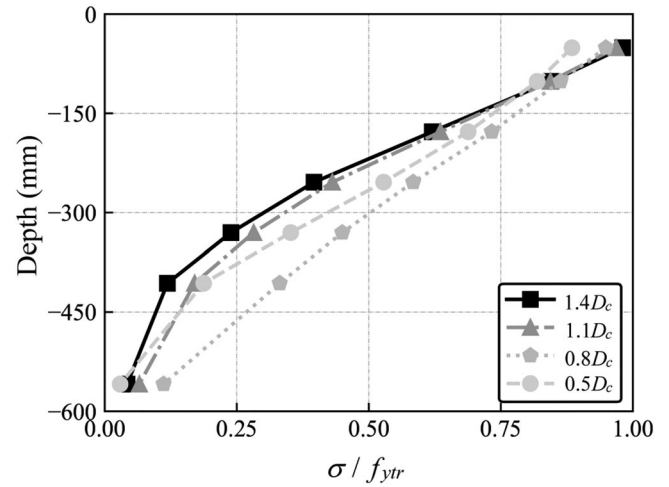


FIGURE 17 Comparison of stress distribution of shaft stirrups with various embedment depths.

transition region for embedment depths beyond  $0.8D_c$ , while a linear distribution is observed for an embedment depth of  $0.5D_c$ . To sum up, shaft stirrup stress distribution depends on the radial stiffness of the cylinder shaft wall around the socket hole. The cylinder shaft wall with a  $D_s/D_c$  less than 1.5 and an embedment depth beyond  $1.1D_c$  performs small radial stiffness, leading to a parabolic stress distribution among shaft stirrups. Regarding the cylinder shaft wall with a  $D_s/D_c$  beyond 1.6 and an embedment depth below  $0.8D_c$ , the linear stress distribution is observed because of large radial stiffness.

#### 4.3 | Shaft stirrup ratio

Figure 18 exhibits the backbones of FE models with shaft stirrup ratios of 0.28%, 0.40%, 0.53%, and 0.81%,



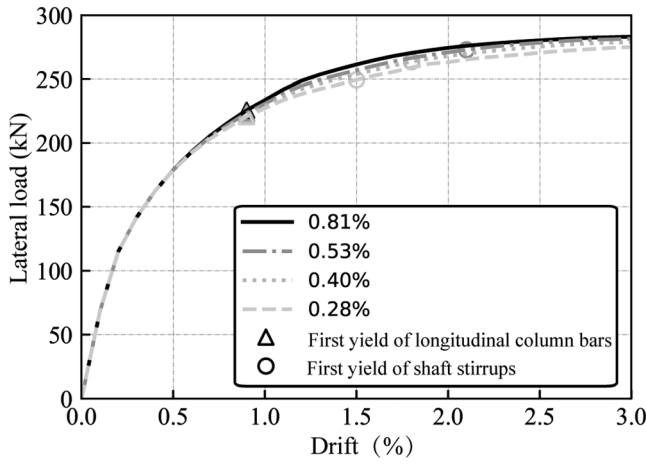


FIGURE 18 Comparison of backbone curves with various shaft stirrup ratios.

corresponding to 35%, 50%, 65%, and 100% of that at the column base, respectively. Caltrans seismic design criteria<sup>8</sup> specify that the minimum shaft stirrup ratio of the transition region is recommended as 50% of that required at the base of the column. However, Figure 18 shows that the minimum shaft stirrup ratio should be 100% of that required at the column base to avoid the yielding of shaft stirrups, which emphasizes the necessity of detailed design for the shaft stirrup ratio. In addition, numerical results indicate that the shaft stirrup ratio has little effect on the mechanical behavior of the transition region before the first yielding of longitudinal column reinforcements, which is consistent with the finding reported by Cheng et al.<sup>14</sup>

## 5 | MODIFIED STM MODEL

### 5.1 | STM model layout

Based on the aforementioned analysis, a novel STM is proposed for the seismic design of column-to-drilled shaft connections, as shown in Figure 19. It assumes that a two-dimensional STM can describe the force-transfer mechanism in the transition region.<sup>9,10,29,30</sup> Boundary forces (i.e.,  $C_c$ ,  $T_c$ ,  $C_s$ , and  $T_s$ ) and their locations (i.e.,  $x_{cc}$ ,  $x_{tc}$ ,  $x_{cs}$ , and  $x_{ts}$ ) are determined by sectional moment-curvature analysis. An auto moment-curvature analysis program coded by the first author<sup>31</sup> is used in this study (<https://github.com/Penghui0616/MCAnalysis>). The column and shaft sections are discretized into mild longitudinal reinforcement, cover concrete, and core concrete fibers. In particular, the axial stress-strain relationship of concrete is modeled by uniaxial material *Concrete04* in the *OpenSeesPy* platform,<sup>32–34</sup> corresponding to the

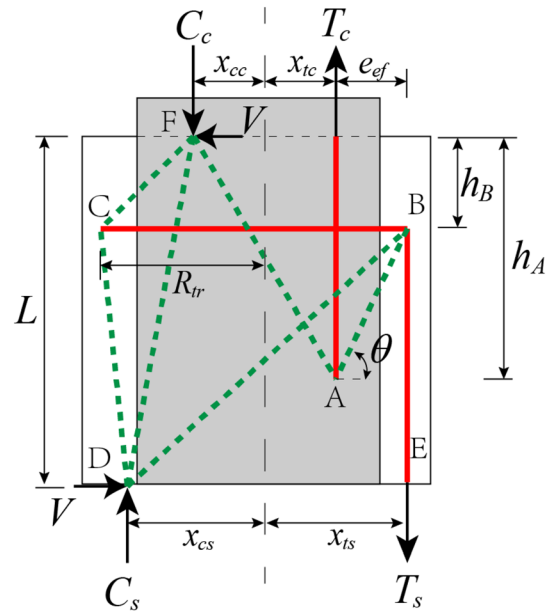


FIGURE 19 Proposed strut-and-tie model.

Mander model.<sup>35</sup> The longitudinal steel reinforcements are simulated using uniaxial material *ReinforcingSteel*. After the moment-curvature analysis of the column, the design shear force  $V$  is determined through the equation of  $M_c/h$ , where  $M_c$  is the flexure capacity of the column section. In accordance with the ductility design criteria, the shaft section is analyzed with a moment of  $M_c + VL$ . The transition depth  $L$  is determined as the minor one of column embedment depth  $h_e$  and tension development depth of longitudinal column bars. The inclination of diagonal struts between spliced bars is assumed to be  $45^\circ$ , following the previous investigation.<sup>16,19</sup> The tension development depth can thus be estimated as  $l_d + s + c$ . The tension development length  $l_d$  for well-confined bars is obtained by the formulation proposed by Murcia-Delso and Fawaz<sup>36</sup>:

$$l_d = \frac{f_{yl} d_{col}}{4\tau_e} + \frac{(f_{ul} - f_{yl}) d_{col}}{4\tau_p}, \quad (13)$$

where  $\tau_e$  and  $\tau_p$  are average elastic bond stress and post-yield bond stress, which are set as  $0.31f_c^{0.75}$  (MPa) and  $0.23f_c^{0.75}$  (MPa), respectively;  $f_{yl}$  and  $f_{ul}$  are yield and ultimate strength of longitudinal column reinforcements.

Node B is located at a depth of the centroid of the shaft stirrup resultant force. A parabolical stirrup stress distribution is assumed since column-to-drilled shaft connections with a  $D_s/D_c$  beyond 1.6 and a column embedment depth below  $0.8D_c$  are not commonly used in engineering practice. Therefore, the depth of node B is approximately  $L/4$  for uniform shaft stirrup distribution.



When stirrup densification is adopted at the top of the shaft, the depth of node B can be rewritten as:

$$h_B = \frac{\sum_{i=1}^{n_s} (L - h_i)^2 h_i}{\sum_{i=1}^{n_s} (L - h_i)^2}, \quad (14)$$

where  $n_s$  is the number of shaft stirrup turns over the transition length  $L$ ;  $h_i$  is the depth of  $i$ -th turn of shaft stirrup. The depth of node A can be determined according to the depth of node B, the horizontal distance between  $T_c$  and  $T_s$ , and the inclination of the strut AB, are given as follows:

$$h_A = h_B + e_{ef} \tan \theta. \quad (15)$$

It is worth noting that the internal force of the strut BD may be negative if the shear span-to-depth ratio is large enough, and bond failure at the tensile side occurs earlier than prying failure. As a result, it is more reasonable to adopt a moment-dominant STM in which strut BD is eliminated, and struts CE and DE are added. In engineering practice, drilled shafts are competitive for bridges with a span below 30 m and a column height below 10 m considering economy and constructability, and the commonly used column diameter is 1.0–1.8 m.<sup>37</sup> So the shear span-to-depth ratio is usually less than 10. Therefore, only the shear-dominant STM is considered in this study.

## 5.2 | Inclination of strut AB

Figure 20a indicates the tensile force-transfer mechanism between column and shaft longitudinal bars. For the  $i$ -th longitudinal column bar, the internal force of the resultant diagonal strut can be decomposed into vertical and radial components, denoted as  $F_{vi}$  and  $F_{ri}$ .  $F_{vi}$  is balanced by the tensile force in longitudinal shaft bars.  $F_{ri}$  is

resisted with the shaft stirrups. The resultant strut force is proportional to the tensile force of the longitudinal column bar, expressed as  $kq_i$ . Because the inclination of the resultant diagonal strut is assumed to be  $45^\circ$ , the magnitude of  $F_{ri}$  is equal to  $kq_i \cos 45^\circ$ . As a result, radial force distribution is the same as that of the tensile force of longitudinal column bars, as shown in Figure 20b. To simplify the three-dimensional structure into a two-dimensional STM, the STM only accounts the horizontal component of  $F_{ri}$  in  $x$  direction. So the inclination of strut AB can be expressed as:

$$\theta = \arctan \frac{\sum_{i=1}^{n_t} F_{vi}}{\sum_{i=1}^{n_t} F_{xi}} = \arctan \frac{\sum_{i=1}^{n_t} q_i}{\sum_{i=1}^{n_t} q_i \cos \alpha_i} = \arctan \frac{R'_c \sum_{i=1}^{n_t} q_i}{\sum_{i=1}^{n_t} q_i x_i}, \quad (16)$$

where  $n_t$  is the number of longitudinal column bars in the tensile region;  $R'_c$  is the distance between the centroids of the column and the longitudinal column bar. Realizing  $\sum_{i=1}^{n_t} q_i x_i / \sum_{i=1}^{n_t} q_i = x_{tc}$ , the inclination of strut AB can be rewritten as:

$$\theta = \arctan \frac{R'_c}{x_{tc}}. \quad (17)$$

## 5.3 | Stress distribution in shaft stirrups

As discussed in Section 3.4, the peak value of stirrup stress appears in the front of the loading direction. However, the tie force  $F_{BC}$  represents the resultant stirrup force at the intersection of the  $y$  axis and the stirrup. It is necessary to reveal the stress distribution along shaft stirrups. A tiny deformation of  $\Delta x$  is supposed to occur in the column, as shown in Figure 21a. The displacement  $\Delta x$  can be decomposed into radial and tangential components, denoted as  $\Delta x_r$  and  $\Delta x_t$ .  $\Delta x_r$  can be expressed as:

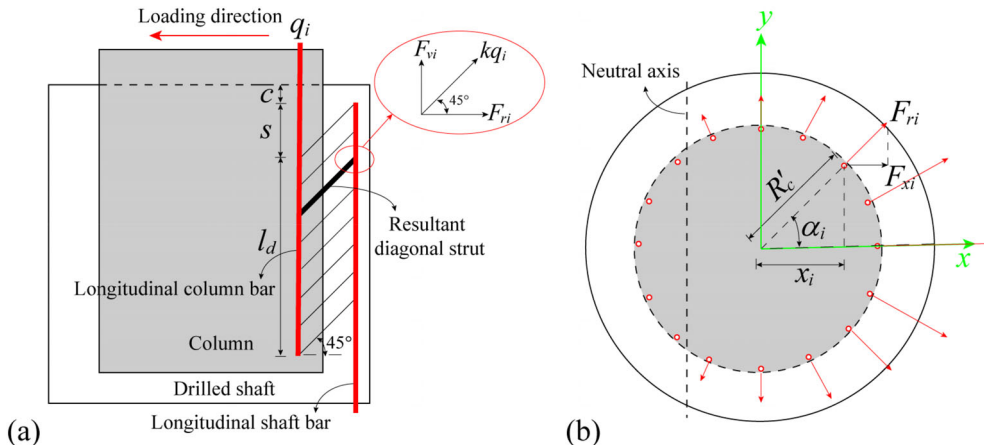
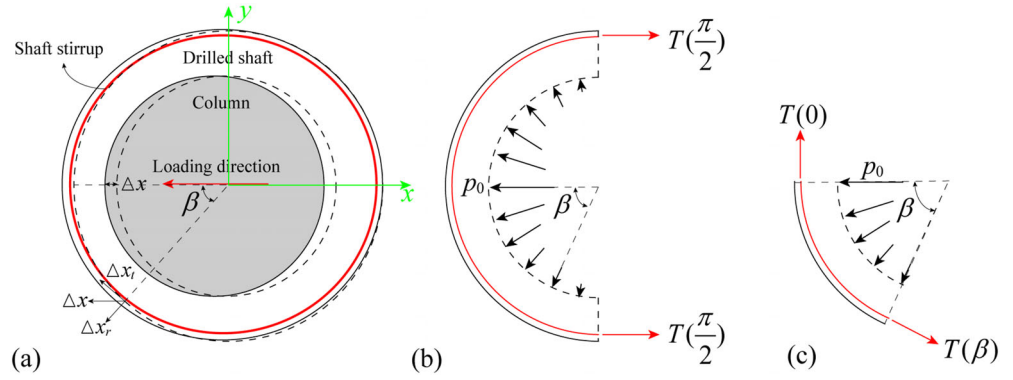


FIGURE 20 Determination of inclination  $\theta$ : (a) force-transfer mechanism between spliced bars; (b) distribution of radial force  $F_{ri}$  among the tensile shaft side.

**FIGURE 21** Stress distribution in shaft stirrups: (a) section of the transition region after deformed; (b) compressive stress applied to the cylinder shaft wall; (c) free body with a central angle of  $\beta$ .



$$\Delta x_r = \Delta x \cos \beta. \quad (18)$$

Assuming the radial stiffness of the cylinder shaft wall is identical among the circumference, the compressive stress induced by extrusion between the embedded column and shaft can be expressed as Equation (19).

$$p(\beta) = p_0 \cos \beta, \quad (19)$$

where  $p_0$  is the compressive stress in the front of the loading direction. Tensile stress induced by the tangential deformation  $\Delta x_r$  is not considered since the bond stress of smooth shaft stirrups is small and reduces with the concrete cracking. Regardless of the tensile strength of concrete, Equation (20) is obtained considering the equilibrium of half cylinder in  $x$  axis, as illustrated in Figure 21b.

$$\int_0^\pi R_{tr} p(\beta) \cos \beta d\beta = 2T\left(\frac{\pi}{2}\right), \quad (20)$$

where  $R_{tr}$  is the radius of shaft stirrups;  $T(\beta)$  is the stirrup stress corresponding to a central angle of  $\beta$ .

Substituting Equation (19) in Equation (20) yields:

$$T\left(\frac{\pi}{2}\right) = \frac{\pi}{4} R_{tr} p_0. \quad (21)$$

Then, Equation (19) is rewritten as:

$$p(\beta) = \frac{4T(\pi/2) \cos \beta}{\pi R_{tr}}. \quad (22)$$

Moreover, Equation (23) is developed in accordance with the equilibrium of the free body shown in Figure 21c.

$$T(\beta) \sin \beta = \int_0^\beta R_{tr} p(\beta) \cos \beta d\beta. \quad (23)$$

Substituting Equation (22) in Equation (23) yields:

$$T(\beta) = \frac{T(\pi/2)}{\pi} \left( \frac{2\beta}{\sin \beta} + \frac{\sin 2\beta}{\sin \beta} \right). \quad (24)$$

So,  $T(\beta)$  approaches  $\frac{4}{\pi} T(\frac{\pi}{2})$  as  $\beta$  approaches 0.

## 5.4 | Shear strength of the transition region

The shear strength of reinforced concrete columns is commonly attributed to the arch and truss mechanism.<sup>38,39</sup> More specifically, the magnitude of the arch action component is taken to be the horizontal component of the diagonal compression strut that forms between the centers of the compression zones at the top and bottom of the transition region. The truss action component, represented by the tensile force of tie BC, includes the contribution of the concrete and stirrups. According to the modified compression field theory,<sup>40,41</sup> AASHTO LRFD specification<sup>7</sup> suggests the concrete component  $V_c$  can be determined as:

$$V_c = 82.97 \eta \sqrt{f_c} A_s, \quad A_s = \frac{0.8 \pi D_s^2}{4}. \quad (25)$$

Equation (25) is to be used with a concrete strength  $f_c$  in MPa, effective shaft section area  $A_s$  in  $m^2$ , and  $V_c$  in kN. The factor  $\eta$  is conservatively set as 2.0 while the minimum amount of transverse reinforcement defined in Equation (26) is satisfied.

$$A_{tr, \min} = 0.083 \sqrt{f_c} \frac{D_s s_{tr}}{f_{ytr}}. \quad (26)$$

As a result, the demand-to-capacity ratio of shaft stirrups is as follows:

$$\frac{\text{Demand}}{\text{Capacity}} = \max \left\{ \frac{(4/\pi)(F_{BC} - V_c)}{2A_{tr}f_{ytr} \sum_{i=1}^{n_s} [(L - h_i)/(L - h_1)]^2}, \frac{A_{tr, \min}}{A_{tr}} \right\}. \quad (27)$$

## 5.5 | Verification of the proposed STM model

The modified STM was validated against experimental results from cases DS2 and DS4, and numerical results

from cases in Section 4. Table 5 summarizes the validation outcomes. It is worth noting that just specimens exhibiting prying failure are considered since the specimens behaving column flexural failure only provide a lower bound on the loading capacity of the transition region. The force demand-to-capacity ratio of shaft stirrups, as well as the ratio of the flexural capacity of column sections  $M_c$  to the maximum moment  $M_{\max}$  obtained by Equation (12), is exhibited. The modified STM is able to reveal the variation tendency of shaft transverse reinforcement demand with the shear

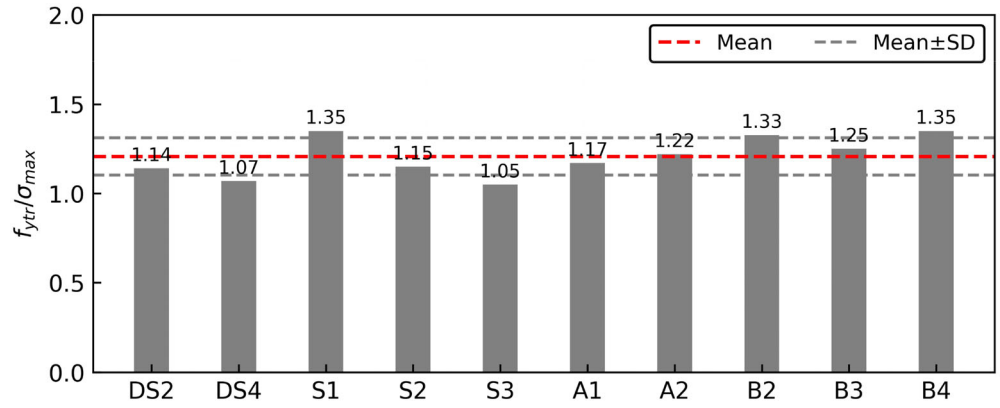
TABLE 5 Model verification against the experimental and numerical results.

Case	$C_c$ (kN)	$T_c$ (kN)	$x_{cc}$ (m)	$x_{tc}$ (m)	$x_{cs}$ (m)	$x_{ts}$ (m)	$L$ (m)	$h_A$ (m)	$h_B$ (m)	$\theta$ (°)	$F_{BC}$ (kN)	Demand Capacity	$\frac{M_c}{M_{\max}}$
DS2	1663	949	0.18	0.09	0.29	0.22	0.71	0.44	0.14	67.7	375	4.16	1.13
DS4	1943	1228	0.18	0.11	0.28	0.22	0.65	0.41	0.15	65.3	571	1.20	1.05
S1	1943	1228	0.18	0.11	0.23	0.19	0.60	0.33	0.14	65.3	715	3.24	1.18
S2	1938	1217	0.18	0.10	0.23	0.19	0.60	0.34	0.14	65.7	509	1.59	1.10
S3	1957	1228	0.18	0.11	0.23	0.19	0.60	0.33	0.14	65.3	444	1.08	1.04
A1	1943	1228	0.18	0.11	0.21	0.17	0.57	0.29	0.14	65.3	800	4.41	1.17
A2	1943	1228	0.18	0.11	0.25	0.21	0.62	0.37	0.15	65.3	638	2.17	1.13
B2	1943	1228	0.18	0.11	0.23	0.19	0.41	0.29	0.10	65.3	663	3.68	1.28
B3	1943	1228	0.18	0.11	0.23	0.19	0.56	0.32	0.13	65.3	708	3.34	1.20
B4	1943	1228	0.18	0.11	0.23	0.19	0.60	0.33	0.14	65.3	715	3.24	1.19
C1	1943	1228	0.18	0.11	0.23	0.19	0.60	0.33	0.14	65.3	714	4.03	1.21
C2	1943	1228	0.18	0.11	0.23	0.19	0.60	0.33	0.14	65.3	715	2.84	1.14
C3	1943	1228	0.18	0.11	0.23	0.19	0.60	0.33	0.14	65.3	716	2.15	1.09
C4	1943	1228	0.18	0.11	0.23	0.19	0.60	0.33	0.14	65.3	718	1.42	1.00

TABLE 6 Evaluation of Chang's STM.

Case	STM mode	$C_c$ (kN)	$T_c$ (kN)	$x_{cc}$ (m)	$x_{tc}$ (m)	$x_{cs}$ (m)	$x_{ts}$ (m)	$L$ (m)	$h_A$ (m)	$h_B$ (m)	$\theta$ (°)	$F_{BC}$ (kN)	Demand Capacity
DS2	V	1663	949	0.18	0.09	0.29	0.22	0.67	0.46	0.15	68.4	303	5.17
DS4	V	1943	1228	0.18	0.11	0.28	0.22	0.64	0.45	0.17	67.0	453	2.41
S1	V	1943	1228	0.18	0.11	0.23	0.19	0.58	0.39	0.20	66.3	638	3.33
S2	V	1938	1217	0.18	0.10	0.23	0.19	0.59	0.40	0.17	68.5	380	1.90
S3	M	1957	1228	0.18	0.11	0.23	0.19	0.59	0.39	0.16	69.3	357	1.69
A1	V	1943	1228	0.18	0.11	0.21	0.17	0.55	0.36	0.21	65.0	788	4.09
A2	V	1943	1228	0.18	0.11	0.25	0.21	0.61	0.42	0.18	66.8	532	2.80
B2	V	1943	1228	0.18	0.11	0.23	0.19	0.41	0.10	0.18	−41.9	−943	/
B3	V	1943	1228	0.18	0.11	0.23	0.19	0.56	0.18	0.19	−9.0	−5885	/
B4	V	1943	1228	0.18	0.11	0.23	0.19	0.58	0.39	0.20	66.3	638	3.33
C1	V	1943	1228	0.18	0.11	0.23	0.19	0.58	0.39	0.20	66.3	638	4.16
C2	V	1943	1228	0.18	0.11	0.23	0.19	0.58	0.39	0.20	66.3	638	2.92
C3	V	1943	1228	0.18	0.11	0.23	0.19	0.58	0.39	0.20	66.3	638	2.21
C4	V	1943	1228	0.18	0.11	0.23	0.19	0.58	0.39	0.20	66.3	639	1.45

**FIGURE 22** Shaft stirrup stress ratios of modified models with shaft stirrup ratios designed by proposed STM. STM, strut-and-tie model.



span-to-depth ratio, diameter ratio of shaft-to-column, and column embedment depth, which is consistent well with the experimental and numerical results. It is worth noticing that the proposed STM is somehow conservative, which can be observed in the analysis result of case C4. It can be explained as follows: (1) the loading capacity predicted by STM is a lower bound of actual loading capacity since STM is based on the lower bound theorem<sup>42</sup>; (2) the conservative factor  $\eta$  leads to underestimation of the concrete contribution to the shear strength.

The inclination of strut AB determined by Equation (17) is approximately  $65^\circ$ , resulting from the simplification of the original three-dimensional problem into a two-dimensional representation. For comparison, the results of the model evaluation using Chang's STM are summarized in Table 6. A similar inclination angle of strut AB was obtained by Chang's models by assuming the depth of points A and B. But the depth estimation is not accurate because a uniform bond stress distribution is assumed, leading to a negative inclination angle of strut AB for specimens B2 and B3, as shown in Table 6. According to the demand-to-capacity ratio of shaft stirrups, Chang's STM is 5%–96% more conservative than the modified STM, which can be attributed to the incorrectly assumed failure mechanism.

In addition, numerical models of each case with shaft stirrup ratio determined by modified STM were reanalyzed, and the maximum shaft stirrup stress  $\sigma_{max}$  of each case was obtained. The change in shaft stirrup ratio was achieved by adjusting the stirrup diameter. The ratios of shaft stirrup yield strength-to-maximum stress, as well as their mean value and standard deviation (SD), are exhibited in Figure 22. The modified STM gives an accurate estimation of the stirrup stress with an average stirrup stress ratio of 1.20 and a coefficient of variation (COV) of only 8.31%.

## 6 | CONCLUSIONS

The CIP drilled shafts are widely utilized in precast bridges. This study aims to reveal the force-transfer mechanism and failure process and propose a simplified design method for column-to-drilled shaft connections between columns and oversized shafts. To this end, detailed finite element models were first developed at the *Diana* platform and validated against previous experimental results. Subsequently, a parametric study was conducted to investigate the effect of shear span-to-depth ratio, diameter ratio of shaft-to-column, column embedment depth, and shaft stirrup ratio. Finally, a modified STM was proposed to design stirrups of the transition region efficiently. The main findings and conclusions are drawn as follows:

- The numerical models generated in the *Diana* platform can precisely simulate the mechanical behavior of column-to-drilled shaft connections. The numerical results matched well with the backbone curves, crack distribution, and bar strain distribution recorded in the quasi-static tests.
- The failure mechanism of column-to-drilled shaft connections is shaft stirrups yield at the compressive side induced by extrusion between the embedded column and shaft. Stirrup stress reaches the peak value in the front of the loading direction.
- The lateral loading capacity of column-to-drilled shaft connections increases with the increase of shear span-to-depth ratio, diameter ratio of shaft-to-column, column embedment depth, and shaft stirrup ratio.
- Shaft stirrup stress distribution depends on the radial stiffness of the cylinder shaft wall around the socket hole. The cylinder shaft wall with a  $D_s/D_c$  less than 1.5 and an embedment depth beyond  $1.1D_c$  performs small radial stiffness, leading to a parabolical stress distribution among shaft stirrups. Regarding the cylinder

shaft wall with a  $D_s/D_c$  beyond 1.6 and an embedment depth below  $0.8D_c$ , the linear stress distribution is observed because of large radial stiffness.

- Based on the observed damage mechanism, a novel STM is proposed in this study for column-to-drilled shaft connections. The modified STM is able to reveal the variation tendency of shaft transverse reinforcement demand with the various design parameters and give an accurate estimation of the stirrup stress with an average stirrup stress ratio of 1.20 and a COV of only 8.31% compared to numerical simulation.

## ACKNOWLEDGMENTS

This research was supported by the National Natural Science Foundation of China under Grant no. 51978511, 51778470, and 52308520. Special thanks to Prof. Marc Eberhard for patiently responding to my detailed questions about the experimental study.

## DATA AVAILABILITY STATEMENT

The data that support the findings of this study are available on request from the corresponding author. The data are not publicly available due to privacy or ethical restrictions.

## ORCID

Penghui Zhang  <https://orcid.org/0000-0002-9518-7079>

## REFERENCES

- Wang X, Luo F, Ye A. A holistic framework for seismic analysis of extended pile-shaft-supported bridges against different extents of liquefaction and lateral spreading. *Soil Dyn Earthq Eng*. 2023;170:107914.
- Wang X, Ye A, Shafieezadeh A, Padgett JE. Fractional order optimal intensity measures for probabilistic seismic demand modeling of extended pile-shaft-supported bridges in liquefiable and laterally spreading ground. *Soil Dyn Earthq Eng*. 2019;120:301–15.
- Zhou L, Ye A, Chen F. Postearthquake vertical load-carrying capacity of extended pile shafts in cohesionless soils: quasi-static test and parametric studies. *J Bridg Eng*. 2022;27(8):04022071.
- Wang X, Shafieezadeh A, Ye A. Optimal EDPs for post-earthquake damage assessment of extended pile-shaft-supported bridges subjected to transverse spreading. *Earthquake Spectra*. 2019;35(3):1367–96.
- Zhou L, Barbato M, Ye A. Experimental investigation of post-earthquake vertical load-carrying capacity of scoured reinforced concrete pile group bridge foundations. *J Bridg Eng*. 2021;26(12):1–14.
- McLean DI, Smith CL. Noncontact lap splices in bridge column-shaft connections. Washington: Washington State Transportation Center; 1997.
- AASHTO. AASHTO LRFD bridge design specifications. Washington, DC, America: American Association of State Highway and Transportation Officials; 2012.
- Caltrans. Caltrans Seismic Design Criteria version 2.0. California, America: California Department of Transportation; 2019.
- Tran HV. Drilled shaft socket connections for precast columns in seismic regions. Washington, DC: University of Washington; 2015.
- Chang MT. Seismic performance of column-to-drilled-shaft connections in reinforced concrete bridges. Washington, DC: University of Washington; 2021.
- Murcia-Delso J, Pui-shum BS, Stavridis A, Liu Y. Required embedment length of column reinforcement extended into type II shafts. California: California Department of Transportation; 2013.
- Lotfizadeh KH. High-strength steel reinforcement in critical regions of earthquake-resistant bridges. California: University of California, San Diego; 2019.
- Masud M. Non-contact lap splices in geometrically dissimilar bridge column to drilled shaft connections. Houston: University of Houston; 2019.
- Cheng Z, Liu D, Li S, Wang J, Zhang J. Performance characterization and design recommendations of socket connections for precast columns. *Eng Struct*. 2021;242:112537.
- Chen H, Masud M, Sawab J, Huang HW, Xu B, Mo YL, et al. Parametric study on the non-contact splices at drilled shaft to bridge column interface based on multiscale modeling approach. *Eng Struct*. 2019;180:400–18.
- Chen H, Masud M, Sawab J, Huang HW, Xu B, Mo YL, et al. Multiscale analysis of non-contact splices at drilled shaft to bridge column interface. *Eng Struct*. 2018;176:28–40.
- Shima H, Chou LL, Okamura H. Micro and macro models for bond in reinforced concrete. *J Fac Eng, Univ Tokyo*. 1987;39(2):133–94.
- Mains RM. Measurement of the distribution of tensile and bond stresses along reinforcing bars. *J Proc*. 1951;48(11):225–52.
- Sagan VE, Gergely P, White RN. Behavior and design of non-contact lap splices subjected to repeated inelastic tensile loading. *Struct J*. 1991;88(4):420–31.
- Tran HV. Drilled shaft socket connections for precast columns in seismic regions. Washington, DC: University of Washington; 2012.
- ASTM. ASTM A82: cold-drawn steel wire for concrete reinforcement. America: American Society for Testing and Materials; 2013.
- Maekawa K, Ishida T, Kishi T. Multi-scale modeling of concrete performance. *J Adv Concr Technol*. 2003;1(2):91–126.
- Selby RG, Vecchio FJ. A constitutive model for analysis of reinforced concrete solids. *Can J Civ Eng*. 1997;24(3):460–70.
- Hordijk DA. Local approach to fatigue of concrete. Delft: Delft University of Technology; 1993.
- Fib. Model Code 2010 – Final draft: volume 1. Lausanne: International Federation for Structural Concrete; 2010.
- Dodd LL, Restrepo-Posada JJ. Model for predicting cyclic behavior of reinforcing steel. *J Struct Eng*. 1995;121(3):433–45.
- Nielsen MP, Hoang LC. Limit analysis and concrete plasticity. 3rd ed. Boca Raton: CRC Press; 2016.
- Zhang P, Yuan W, Wang Z, Qu H. Cost-based optimum design of the earthquake-resistant system for continuous skew overpasses. *Structure*. 2022;45:2051–66.
- Brown DN, Parks JE, Ameli MJ, Pantelides CP. Strut-and-tie models of repaired precast concrete bridge substructures with CFRP shell. *Compos Struct*. 2016;138:161–71.



30. Schlaich J, Schiifer K. Design and detailing of structural concrete using strut-and-tie models. *Struct Eng.* 1991;69(6):113–25.
31. Zhang P, Wang Z, Ge J, Yan X, Liu S. Full-scale experimental study on precast bridge column with grouted sleeve connections and large-diameter reinforcing bars. *Eng Struct.* 2023;294:116747.
32. McKenna F. OpenSees: a framework for earthquake engineering simulation. *Comput Sci Eng.* 2011;13(4):58–66.
33. Zhu M, McKenna F, Scott MH. OpenSeesPy: python library for the OpenSees finite element framework. *SoftwareX.* 2018;7:6–11.
34. Guo J, Ye A, Wang X, Guan Z. OpenSeesPyView: python programming-based visualization and post-processing tool for OpenSeesPy. *SoftwareX.* 2023;21:101278.
35. Mander JB, Priestley MJN, Park R. Theoretical stress-strain model for confined concrete. *J Struct Eng.* 1988;114(8):1804–26.
36. Murcia-Delso J, Fawaz G. Analytical model for bar slip and pull-out capacity of straight bars. *ACI Struct J.* 2019;116(5):137–49.
37. Zhou L. Probability-based performance and post-earthquake functionality assessment for pile supported bridges under combined effects of scour and earthquake hazards. Shanghai: Tongji University; 2022.
38. Khuntia M. Mechanics of concrete participation in cyclic shear resistance of RC. *J Struct Eng.* 1999;125(5):573–4.
39. Kowalsky MJ, Priestley MJN. Improved analytical model for shear strength of circular reinforced concrete columns in seismic regions. *ACI Struct J.* 2000;97(3):243–5.
40. Vecchio FJ, Collins MP. The modified compression-field theory for reinforced concrete elements subjected to shear. *ACI J.* 1986;83(2):219–31.
41. Bentz EC, Vecchio FJ, Collins MP. Simplified modified compression field theory for calculating shear strength of reinforced concrete elements. *ACI Struct J.* 2006;103(4):614.
42. Schlaich J, Schaefer K, Jennewein M. Toward a consistent design of structural concrete. *PCI J.* 1987;32(3):74–150.



**Lianxu Zhou**, Postdoctoral Fellow, School of Engineering, University of British Columbia, Kelowna, BC V1V 1V7, Canada. Email: [lianxu.zhou@ubc.ca](mailto:lianxu.zhou@ubc.ca)

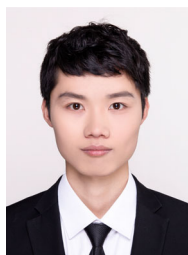


**Junjun Guo**, Postdoctoral Fellow, Department of Bridge Engineering, Tongji University, 1239 Siping Road, Shanghai 200092, China. Email: [guojj@tongji.edu.cn](mailto:guojj@tongji.edu.cn)



**Zhiqiang Wang**, Associate Professor, Department of Bridge Engineering, Tongji University, 1239 Siping Road, Shanghai 200092, China. Email: [wangzhiq@tongji.edu.cn](mailto:wangzhiq@tongji.edu.cn)

## AUTHOR BIOGRAPHIES



**Penghui Zhang**, Ph.D. Candidate, Department of Bridge Engineering, Tongji University, 1239 Siping Road, Shanghai 200092, China. Email: [penghui@tongji.edu.cn](mailto:penghui@tongji.edu.cn)

**How to cite this article:** Zhang P, Zhou L, Guo J, Wang Z. Strut-and-tie model for column-to-drilled shaft connections in reinforced concrete bridge columns subjected to lateral loads. *Structural Concrete.* 2024. <https://doi.org/10.1002/suco.202400098>